NPG Asia Materials (2015) 7, e178; doi:10.1038/am.2015.32
© 2015 Nature Publishing Group All rights reserved 1884-4057/15
www.nature.com/am

ORIGINAL ARTICLE

Hyper-dendritic nanoporous zinc foam anodes

Mylad Chamoun[1,2,5], Benjamin J Hertzberg[2], Tanya Gupta[2], Daniel Davies[2], Shoham Bhadra[3], Barry Van Tassell[4], Can Erdonmez[1] and Daniel A Steingart[2]

The low cost, significant reduction potential and relative safety of the zinc electrode is a common hope for a reductant in secondary batteries, but it is limited mainly to primary implementation due to shape change. In this work, we exploit such shape change for the benefit of static electrodes through the electrodeposition of hyper-dendritic nanoporous zinc foam. Electrodeposition of zinc foam resulted in nanoparticles formed on secondary dendrites in a three-dimensional network with a particle size distribution of 54.1–96.0 nm. The nanoporous zinc foam contributed to highly oriented crystals, high surface area and more rapid kinetics in contrast to conventional zinc in alkaline mediums. The anode material presented had a utilization of ~88% at full depth-of-discharge (DOD) at various rates indicating a superb rate capability. The rechargeability of Zn^0/Zn^{2+} showed significant capacity retention over 100 cycles at a 40% DOD to ensure that the dendritic core structure was imperforated. The dendritic architecture was densified upon charge–discharge cycling and presented superior performance compared with bulk zinc electrodes.

NPG Asia Materials (2015) **7,** e178; doi:10.1038/am.2015.32; published online 24 April 2015

INTRODUCTION

Zinc has a rich history as an anode for static,[1,2] redox,[3,4] semi-solid[5,6] and flow assisted cells,[7] and remains attractive for secondary applications despite the current popularity of lithium ion batteries due to its abundance, safety and scalability. Historically, it has been limited by morphological uncertainty, which is dependent on local current density and pH.[8] Two typically undesirable regimes are ramification or the formation of dendrites that lead to electrical-short-circuits[9] and precipitation of ZnO[10,11] that can irreversibly passivate a surface. In conventional static zinc systems (composites, pastes and powders), these mechanisms lead to terminal failure, and in flow and flow-assisted cells they can be reversed only at the cost of additional system overhead.

In this work, we present a method of synthesizing zinc foam electrochemically, *in situ*. The formation of zinc foam *in situ* may enable new possibilities of designing structural electrodes because of the freedom of shape and the advantage of replacing depleted or contaminated electrolyte for long-life usage. The zinc foam proposed in this paper is formed by a three-dimensional network of dendrites that is electrochemically active and electronically conductive, at the nanoscale. We find that the nanoporous zinc structure presents a modified activation energy for electrochemical cycling. Conductive paths throughout the internal structure result in a more uniform current distribution, reducing non-uniform concentration gradients and anode polarization losses.[12] We exploit the dendrites, which are normally a limitation against rechargeable zinc electrodes, by initially operating at states far from equilibrium (cathodic overpotentials from ~200 to ~600 mV) and thereafter cycling toward equilibrium. This presents a rethinking of the process of recharging batteries. The dendritic network, upon recharging a battery at standard operating conditions, may densify the architecture over cycles and suppress initiation of dendrites if the three-dimensional core is kept intact. Recent work has indicated that zinc structures with submicron features can undergo 50 charge–discharge cycles without failure.[13] Here, we describe a simple mechanism for making such structures, with the option to alter the surface kinetics as a function of process regime.

We investigated the electrodeposition of zinc with hydrogen at different overpotentials by characterizing its electrochemical and morphological properties. We studied the kinetics of the produced material via electrochemical techniques such as chronocoulometry and Butler-Volmer modeling. We characterized the morphology of zinc by scanning and transmission electron microscopy methods. We determined the particle size distribution and specific surface area of zinc foam through X-ray diffraction, differential scanning calorimetry and BET (Brunauer-Emmet-Teller) techniques. Finally, we investigated the reversibility of Zn^0/Zn^{2+} redox chemistry and discharge-rate capability of the material for battery applications. The hyper-dendritic zinc electrode showed significant capacity retention over 100 cycles, and due to the electrochemical synthesis procedure, it can be reformed *in situ* if needed.

MATERIALS AND METHODS

Experiments carried out in alkaline conditions where 8.9 M KOH pellets (Sigma-Aldrich, St Louis, MO, USA) and 0.61 M ZnO (Sigma-Aldrich) were dissolved in

---

[1]Brookhaven National Laboratory, Sustainable Energy Technologies Department, Upton, NY, USA; [2]Department of Mechanical and Aerospace Engineering, Andlinger Center for Energy and the Environment, Princeton University, Princeton, NJ, USA; [3]Department of Electrical Engineering, Andlinger Center for Energy and the Environment, Princeton University, Princeton, NJ, USA and [4]Department of Chemical Engineering, City College of New York, New York, NY, USA
[5]Current address: Department of Materials and Environmental Chemistry, Arrhenius Laboratory, Stockholm University, S-106 91 Stockholm, Sweden.
Correspondence: Professor DA Steingart, Department of Mechanical and Aerospace Engineering, Andlinger Center for Energy and the Environment, Princeton University, D428 EQuad, Princeton, NJ 08544, USA.
E-mail: steingart@princeton.edu

Received 30 October 2014; revised 19 January 2015; accepted 25 February 2015

deionized (DI) water and stirred overnight. The zinc foam was prepared electrochemically from flooded undivided cells containing 10 ml of electrolyte in a three-electrode setup that was controlled by a potentiostat (Keithley Model 2401 Low Voltage SourceMeter Instrument, Keithley Instruments Inc., Cleveland, OH, USA). The setup consisted of a 0.5-mm diameter platinum wire (Sigma-Aldrich) working electrode, an Hg/HgO reference electrode (Koslow Scientific Company, Englewood, NJ, USA) and a nickel mesh (Dexmet Corporation, Wallingford, CT, USA) that served as a counter electrode. Electrodeposited zinc on a platinum wire was controlled with a defined charge passed of 100 coulombs (C), using a controlled-potential coulometry method and a surface area of 0.260 cm^2. For studies of the rechargeability of the zinc foam, the working electrode was prepared with a charge passed of 3000 C, and a conventional nickel electrode with excess capacity served as the counter electrode. The platinum electrode was initially activated and cleaned by dipping it in nitric acid (Sigma-Aldrich) for 1 h at 60 °C, and then rinsed with DI water. The nickel electrode was prepared by mixing a slurry consisting of 50 wt.% NiOOH (Sigma-Aldrich), 40 wt.% graphite (Timcal Timrex KS6, Imerys Graphite & Carbon, Bodio, Switzerland) and 10 wt.% PTFE (Sigma-Aldrich), and the resulting paste onto a flat surface using a rolling pin. The rolled electrode was then dried in a vacuum oven at 125 °C for 2 h. The assembly was compressed in a uniaxial press using 4 tons of force on a nickel mesh current collector. The full cell was sandwiched between two layers of non-woven cellulose membrane (Freudenberg), and topped up with either 10 ml electrolyte for flooded cells or 1 ml electrolyte for non-flooded cells. The uncompensated resistance, R_u, was evaluated for each setup in this work through a current interrupt method. The R_u values obtained were under 4 Ω for all methods and hence neglected, due to the absence of any significant effect on the measured potential. For *in situ* studies, the zinc was kept in solution. For *ex situ* studies, the sample was rinsed three times in 8.9 M KOH to ensure the dissolution of ZnO, neutralized with DI water five times, and then dried under vacuum for 1 h at 110 °C. The samples were prepared by grinding with mortar, pestle and small amounts of acetone until a fine powder was obtained. Purum bulk zinc powder (Sigma-Aldrich) was used as a standard comparison. The Tafel studies were carried out using a 0.5-mm thick zinc foil with a surface area of 0.260 cm^2 (Sigma-Aldrich) cleaned in 10 wt.% sulfuric acid (Sigma-Aldrich) and rinsed with DI water.

Scanning electron microscopy (SEM) images and elemental composition quantifications were assessed by an FEI Quanta 200 FEG Environmental SEM (FEI, Hillsboro, OR, USA) connected with an integrated electron diffraction

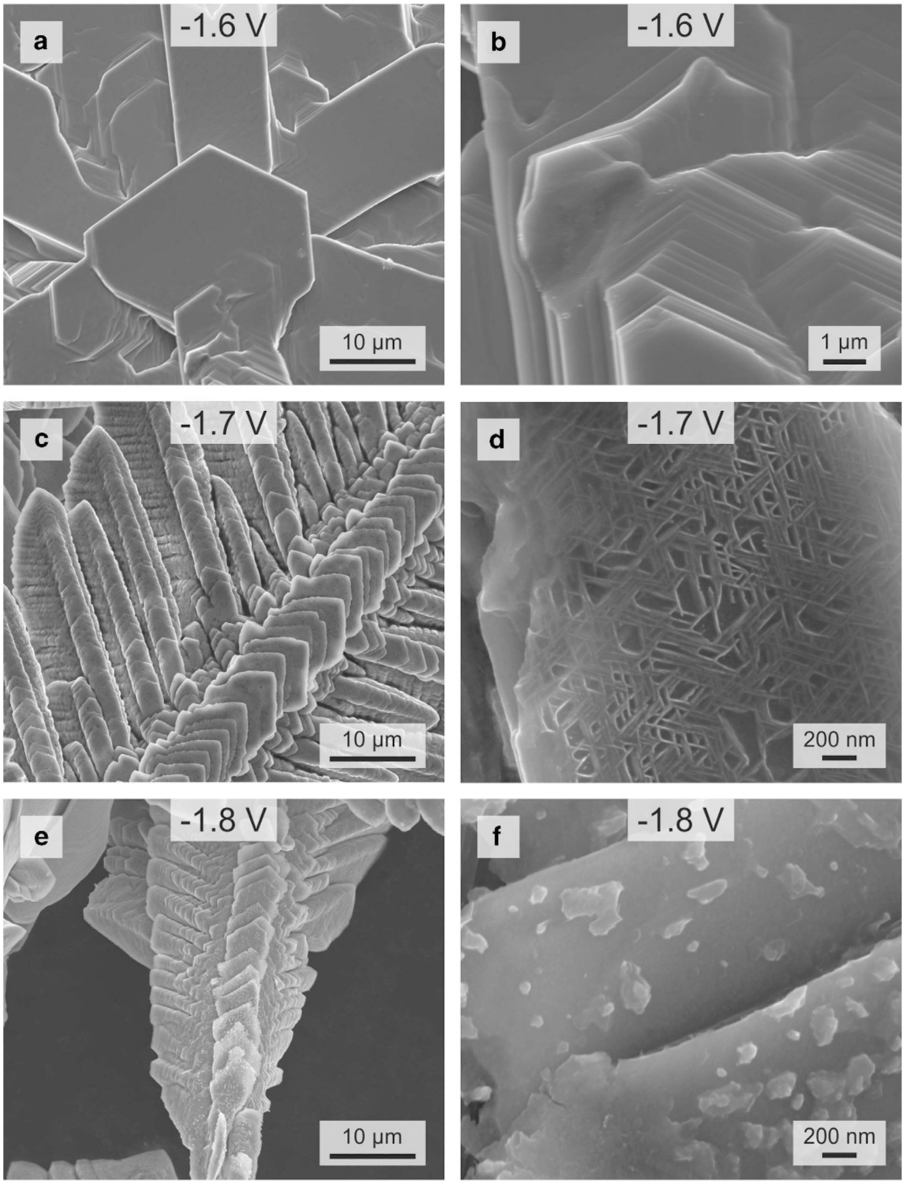

Figure 1 SEM images of electrodeposited zinc in alkaline solution at (**a** and **b**) − 1.6 V, (**c** and **d**) − 1.7 V, (**e** and **f**) − 1.8 V, (**g** and **h**) − 1.9 V and (**i** and **j**) − 2.0 V vs Hg/HgO.

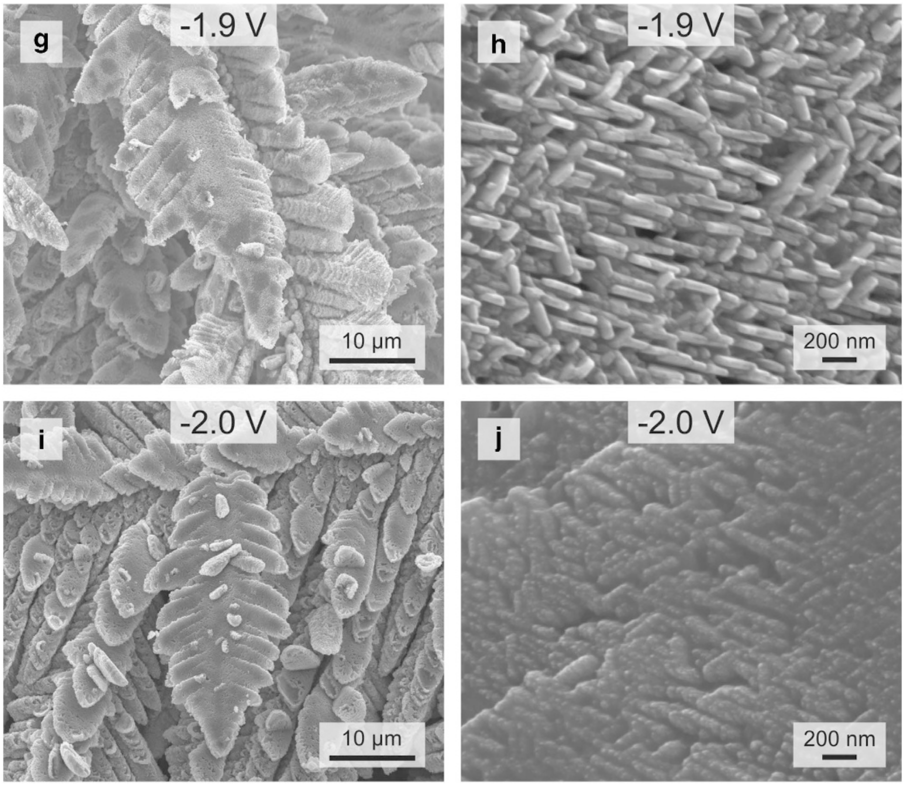

Figure 1 Continued.

spectroscopy system. High-resolution transmission electron microscopy (TEM) images were taken by a Philips CM200 FEG-TEM operating at an accelerating voltage of 200 kV. The samples were attached onto a lacey carbon support film on a gold 200 mesh grid (Electron Microscopy Sciences, Hatfield, PA, USA). An OptixCam OCS-1.3 optical microscope (The Microscopic Store, LLC, Roanoke, VA, USA) was used to image the zinc foam growth on a nickel mesh current collector. BET surface area measurements were carried out using a Micromeritics ASAP 2010 apparatus (Micromeritics Instrument Corporation, Norcross, GA, USA) using nitrogen as an adsorbent. The samples were prepared by heating overnight at 120 °C while flowing N_2 gas. The N_2 adsorption was measured from a relative pressure range of 0.01–1 at 77.3 K. Differential scanning calorimetry (DSC) measurements were performed using a PerkinElmer Pyris 1 DSC (PerkinElmer Inc., Waltham, MA, USA) with a process scheme of rapid isothermal treatment to 340 °C in 5 min and then heated at rate of 1 °C/min up to 440 °C at ambient pressure in argon atmosphere. High resolution X-ray diffraction patterns were taken at room temperature with a Bruker D8 Discover X-ray Diffractometer (Bruker Corporation, Billerica, MA, USA) and in 0.2° intervals with 1 s settling time using a Cu-Kα source operating at 40 kV and 40 mA.

RESULTS AND DISCUSSION

Zinc metal is soluble in strong alkaline solutions and equilibrates with zincate ions, $Zn(OH)_4{}^{2-}$, at pH values >12. The charge and discharge reaction of zinc electrodes, the precipitation of ZnO at supersaturated concentration of zincate ions and hydrogen evolution are shown in equations (1), (2) and (3), respectively:[14,15]

$$Zn_{(s)} + 4OH^- \leftrightarrow Zn(OH)_4^{2-}(aq) + 2e^- \tag{1}$$

$$Zn(OH)_4^{2-}(aq) \leftrightarrow ZnO_{(s)} + H_2O_{(l)} + 2OH^- \tag{2}$$

$$H_2O_{(l)} + 2e^- \leftrightarrow H_2(g) + 2OH^- \tag{3}$$

Zinc has an equilibrium potential that is about 0.4 V lower than the equilibrium potential of hydrogen evolution at pH 14 thus having a direct influence on the efficiency of electrodeposited zinc.

Electrodeposited zinc foam on platinum at 100 C charge passed and different potentials is included with the Supplementary Information. The metallic foam structure was achieved at potentials applied above − 1.6 V and a substantial amount of hydrogen evolved with zinc foam was observed at − 2.0 V. Figure S1 in the Supplementary Information shows that the measured current increased more rapidly at higher applied potentials, despite being well beyond the limiting current for zinc in this electrolyte. The increase in current over time was most likely due to increased surface: while reaction (3) is competitive with reaction (1), we found in all described experiments coulombic efficiencies of 84.9 ± 3.1%, indicating a similar fraction of current formed $H_2(g)$ at each test.

Electrodeposited zinc has been reported as mossy, epitaxial layers, boulder-like and dendritic morphologies at low to high overpotentials.[7,9,16–18] The morphology of electrodeposited zinc is dependent on the intermediate product zincate. Precipitation of zincate at the surface interface generally initiates dendritic morphologies at limiting current densities due to non-uniform concentration gradients. Effort on controlling mass transport by convection was carried out by Ito *et al.*[7] where they quantified the change in morphology of deposited zinc. In this work, we mainly operated at limiting current densities with no convection control at high overpotentials. Hexagonal crystals organized into fernlike dendrites with particles sized between 2 and 10 μm are shown in Figures 1a–d. At high cathodic overpotentials ($> \sim 500$ mV, assuming an equilibrium potential of zinc at − 1.38 V), oriented zinc pillars were formed at nanoscale, seen in Figures 1h and j, with a mean particle size

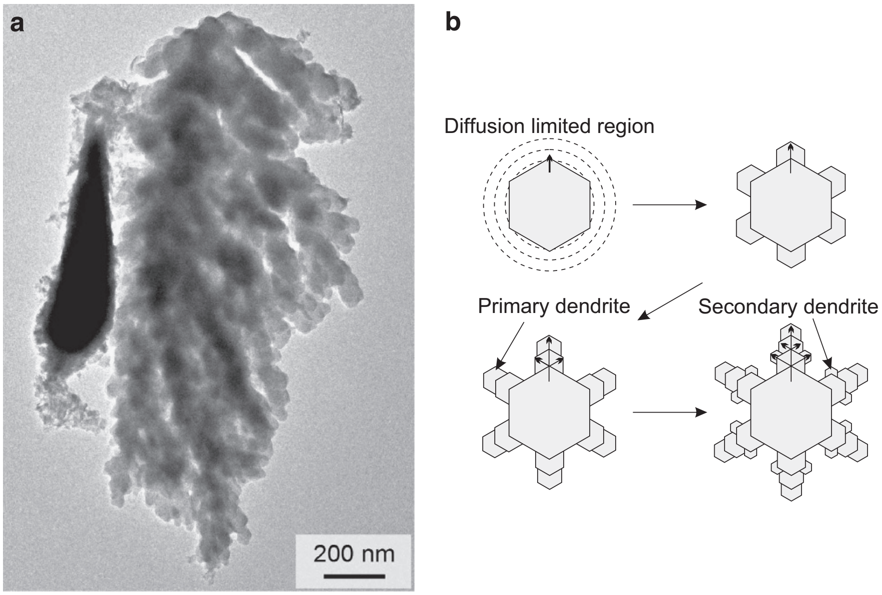

Figure 2 (**a**) TEM image taken at nanoscale of electrochemical deposited hyper-dendritic porous zinc foam formed at −2.0 V vs Hg/HgO. (**b**) Scheme of zinc dendrite formation based on the diffusion-limited aggregation model.

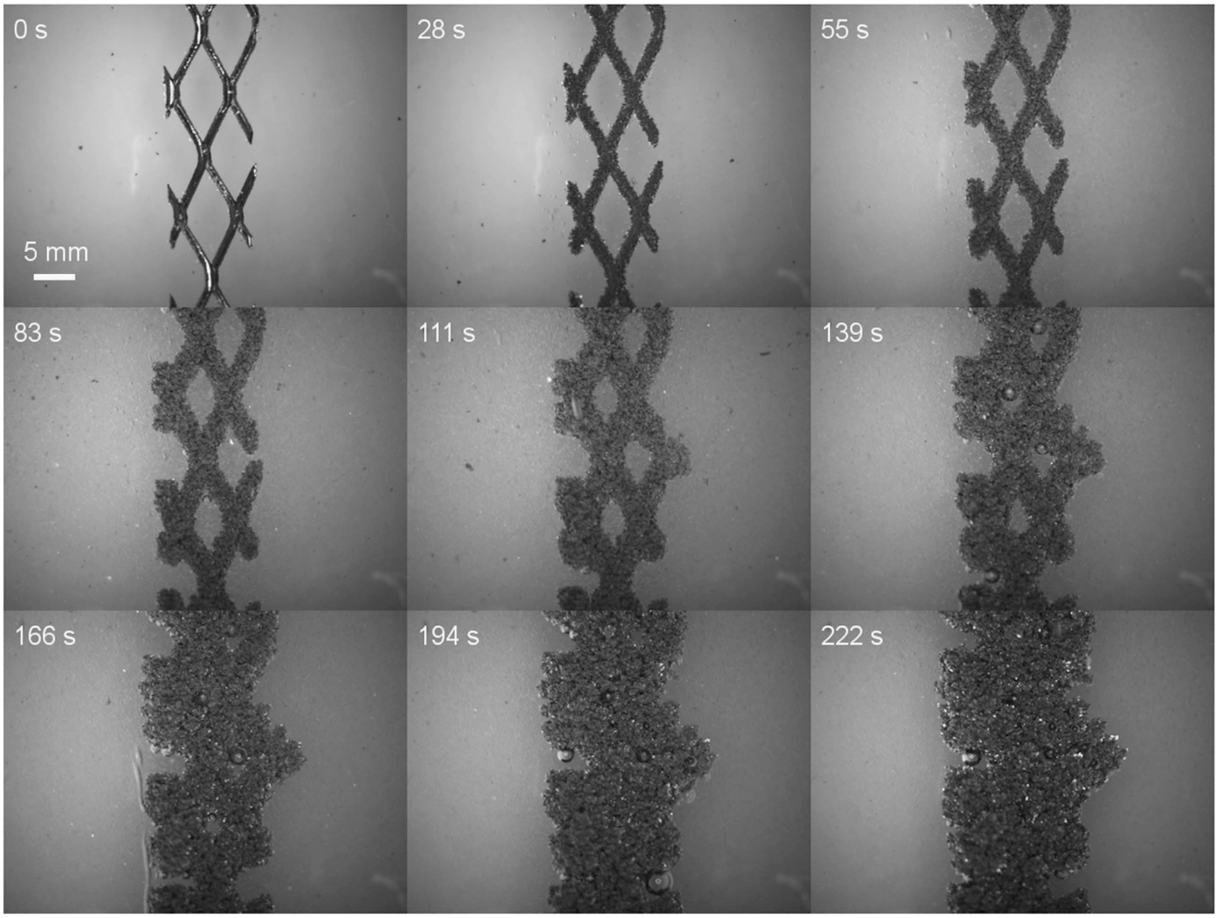

Figure 3 Time-lapse microscopy movie of hyper-dendritic zinc foam growth on a nickel mesh current collector at −2.0 V vs Hg/HgO in a chronological order, from top left to bottom right.

of 73.05 ± 8.95 nm measured from 49 randomly selected zinc particles. At higher overpotentials, transport rate of zincate ions, $Zn(OH)_4{}^{2-}$ will be limited at the surface-liquid interface, causing unpredictable growth of primary and secondary dendrites.

The elemental composition of the samples in Figure 1 was analyzed with EDS. A small amount of the oxide was formed: 3.2, 3.8, 5.9, 6.5 and 8.2 wt.%, in increasingly negative potentials, respectively. The amount of potassium was below 0.6 wt.% for all measurements thus negligible. This supports our expectation that the majority of the deposited foam was metallic zinc. The hyper-dendritic nanoporous zinc foam prepared at − 2.0 V was further investigated under a TEM. The TEM image taken of hyper-dendritic nanoporous zinc foam is seen in Figure 2a. A schematic representation of our interpretation of zinc dendrite formation, based on the diffusion-limited aggregation model[19–21] is seen in Figure 2b. Our hypothesis is that branch growth on secondary dendrites at the edge of the primary dendritic spines led to the formation of nanoporous zinc. The growth of these branches may be the cause of three-dimensional threadlike networks consisting of zinc particles. López and Choi[12] presented a similar result of stabilized dendrite growth forming motif crystals that were interconnected in a matrix with dendritic backbones. A mean particle size of 72.15 ± 18.05 nm was assessed from the TEM image based on 72 randomly selected zinc nanoparticles. Typical 'large' zinc hexagonal crystals were no longer evident due to the initiation of numerous branches resulting in spherical boundaries, but rather we see small defective zinc hexagonal aggregates.

Of particular note is the way in which the zinc dendritic foam grows. The zinc foam grows in an isotropic manner at the micron scale as shown in the time-lapse movie of zinc foam growth on nickel mesh in Figure 3. At first this is counterintuitive as one expects an 'electrochemical lighting rod' under these conditions, but upon inspection these fast directional growths are occurring, just at the nanometer scale. In concert, the exploitation of the small directional growth from edge facets seems to result in a micron scale morphology of randomly oriented particles. This growth then continues, apparently creating a conformal 'hyper-dendritic' foam.

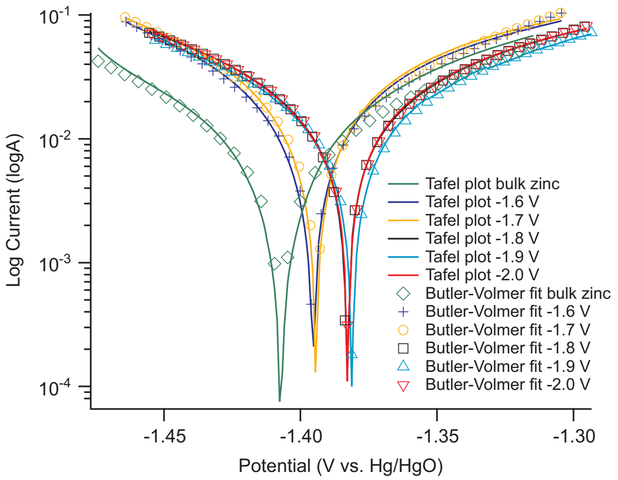

Figure 4 Tafel plot and Butler-Volmer fit of electrodeposited zinc at different potentials and standard bulk zinc. The lines show the experimental data and the markers show the calculated fit.

The kinetics of electrodeposited zinc at varying potentials were evaluated *in operando*, in comparison with a standard bulk zinc sample, by first depositing zinc on platinum at a constant potential with a charge passed of 100 C to ensure a thick layer of deposited metal for all samples. The samples were kept in solution at an open-circuit voltage for 1 h to relax the surface. Afterwards, polarization curves were swept linearly from − 80 to 80 mV in overpotentials at a sweeping rate of $1\ mV\ s^{-1}$. The kinetic parameters of zinc were calculated through the Butler-Volmer equation at electron-transferred limited regions. The Butler-Volmer relationship is seen in (4) where I_0 is the exchange current, η the activation overpotential, α_c the cathodic charge transfer coefficient. Figure 4 shows the measured Tafel plots and Butler-Volmer fits at different potentials. Calculated kinetic parameters are given for the different potentials in Table 1.

$$I = I_0 A\left(\exp\left[\frac{(1-\alpha_C)nF\eta}{RT}\right] - \exp\left[-\frac{\alpha_c nF\eta}{RT}\right]\right) \tag{4}$$

The literature typically concerns kinetic parameters of electrodeposited zinc at low cathodic overpotentials (30–100 mV) in alkaline solutions.[22–29] Cathodic Tafel slope values of ~ $120\ mV\ dec^{-1}$ and cathodic charge transfer coefficient of ~ 0.55 are suggested. The kinetic results evaluated from the Butler-Volmer fit at potentials of electrodeposited zinc at − 1.6 V and the standard bulk zinc is in agreement with the literature.[22–29] At applied potentials above − 1.6 V, more rapid kinetics were evident: we observed an increased exchange current of 36.8 ± 4.3 mA at − 2.0 V in comparison with 12.9 ± 0.5 mA for the standard. In addition to the evidence of more rapid kinetics, the anodic and cathodic Tafel slopes were calculated at 212.9 ± 5.1 and $190.1 \pm 4.7\ mV\ dec^{-1}$ at − 2.0 V in comparison with 125.6 ± 7.5 and $107.3 \pm 1.5\ mV\ dec^{-1}$ for the standard. The kinetic transition led to a lower activation energy at potentials of − 1.8 to − 2.0 V and may have occurred because the nucleation of zinc particles on the edge (branch formation) was more probable than the continuous growth of existing primary dendrites. The anodic reaction, the oxidation of Zn^0 to $Zn(OH)_4{}^{2-}$, was also dominant. The anodic and cathodic charge transfer coefficients of 0.69 ± 0.06 and 0.31 ± 0.06 at − 2.0 V, compared with 0.45 ± 0.01 and 0.55 ± 0.01 for the standard, indicated the oxidation reaction being dominant. A lower equilibrium potential was measured for the samples prepared above the potentials of − 1.8 V ($E_0 = -1.38$ V) in comparison with the ones prepared under potentials of − 1.7 V ($E_0 = -1.395$ V) and the bulk sample ($E_0 = -1.41$ V). Osório *et al.*[30] presented the results of corrosion rates

Table 1 Measured kinetic parameters for electrodeposited zinc from Butler-Volmer fit to Tafel slope at different potentials

Kinetic parameters	*Bulk zinc*	*− 1.6 V*	*− 1.7 V*	*− 1.8 V*	*− 1.9 V*	*− 2.0 V*
I_0 (mA)	12.9 ± 0.5	19.4 ± 1.3	26.1 ± 2.0	34.6 ± 6.7	29.0 ± 5.6	36.8 ± 4.3
α_a (−)	0.45 ± 0.01	0.41 ± 0.02	0.49 ± 0.01	0.67 ± 0.04	0.66 ± 0.04	0.69 ± 0.06
α_c (−)	0.55 ± 0.01	0.59 ± 0.02	0.51 ± 0.01	0.33 ± 0.04	0.34 ± 0.04	0.31 ± 0.06
Anodic Tafel slope (mV/dec)	125.6 ± 7.5	123.5 ± 2.1	144.2 ± 3.8	205.3 ± 7.7	195.6 ± 6.9	212.9 ± 5.1
Cathodic Tafel slope (mV/dec)	107.3 ± 1.5	100.0 ± 1.7	116.3 ± 3.4	179.6 ± 7.0	175.2 ± 5.5	190.1 ± 4.7

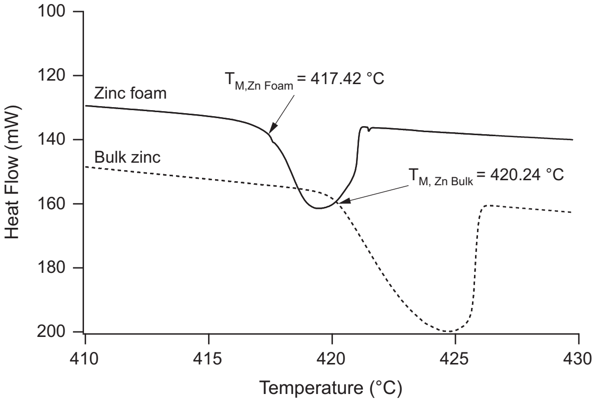

Figure 5 Heat flow vs temperature from DSC measurements of nanoporous zinc foam produced from − 2.0 V vs Hg/HgO (solid line) in comparison with bulk zinc (dashed line). The onset indicated the melting point of both metals.

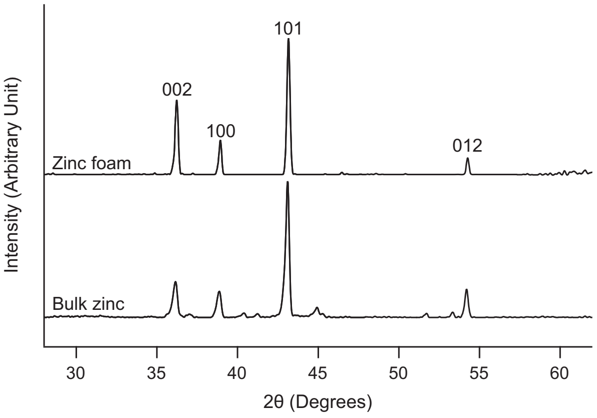

Figure 6 X-ray diffraction patterns (intensity vs *2θ*) of zinc foam and bulk zinc.

as a function of secondary arm spacing for zinc alloys. They concluded that a shorter secondary dendrite arm spacing resulted in an increased amount of hydrogen evolved at equilibrium states for zinc alloys. A more rapid corrosion rate with shorter dendrite arm spacing achieved at increasingly negative potentials was evident for the anode material in this work as well.

The N_2 adsorption–desorption isotherms of electrodeposited hyper-dendritic nanoporous zinc foam at − 2.0 V were measured. A specific surface area of $12.16 \pm 0.62\ m^2\ g^{-1}$ was obtained from the pressure range of $0.05 < P/P_0 < 0.3$. In contrast to bulk zinc, which has a specific surface area of $0.5–1\ m^2\ g^{-1}$, the specific surface area of zinc foam was 10–25 times larger. Assuming the dendrites are composed of solid, spherical particles with smooth surface in narrow size distribution and a theoretical density of $7.14\ g\ cm^{-3}$, a mean particle size diameter of 69.10 nm was calculated from (5) where ρ is the theoretical density in g/cm^3 and S_{BET} is the specific surface area in $m^2\ g^{-1}$. This is in agreement with what was observed in the TEM.

$$D_{BET} = 6000/\rho S_{BET} \tag{5}$$

DSC profiles of prepared hyper-dendritic zinc foam and conventional bulk zinc are seen in Figure 5, presenting a melting-point depression of the zinc foam because of reduction in particle size. The thermograms showed a dip in heat flow, which indicated an endothermic phase transition. A decrease in heat of fusion of the zinc foam, $6.56\ kJ\ mol^{-1}$, in contrast to the bulk zinc, $7.26\ kJ\ mol^{-1}$, was achieved. A melting point for the zinc foam was seen at 417.42 °C and for the bulk zinc at 420.24 °C. A mean particle diameter size of 85.30 nm was calculated based on Gibbs-Thomson thermodynamic model of melting point depression for nanoparticles seen in:

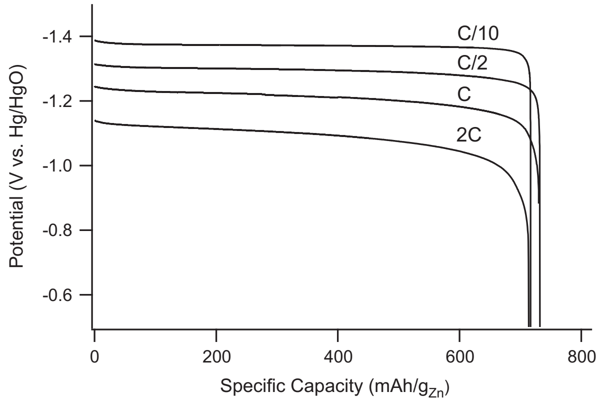

Figure 7 Discharge capacity profiles as a function of rate of the hyper-dendritic nanoporous zinc foam initially prepared *in situ* with charge passed of 3000 C. The discharge rates used are 2C, C, C/2 and C/10.

$$d = \frac{4\gamma_{sl}}{H_f \rho_s \left(1 - \left(\frac{T_M(d)}{T_{MB}}\right)\right)} \tag{6}$$

where γ_{sl} is the solid–liquid interfacial energy in $J\ m^{-2}$, H_f is the bulk heat of fusion in $J\ g^{-1}$, ρ_s is the density of the solid in $g\ m^{-3}$, T_{MB} is the bulk melting temperature in K and $T_M(d)$ is the nanoparticle melting temperature in K. All physical constants were taken from the literature and the melting points were measured from the onset of the endothermic phase transition.[31,32]

X-ray diffraction patterns of prepared zinc foam at − 2.0 V and bulk zinc are presented in Figure 6. The patterns showed highly crystalline zinc with well-defined peaks for zinc corresponding to the lattice planes {002}, {100}, {101} and {012}. No corresponding peaks of ZnO or $Zn(OH)_2$ were found, indicating that pure hexagonal zinc crystals were formed. An increased relative intensity of the peak at 36.29° for the zinc foam (B) compared with the bulk zinc (A) indicates that zinc was preferentially deposited in highly oriented {002} direction. X-ray peak broadening analysis was carried out through the Scherrer equation, seen in (7), which estimates the mean crystallite size from the full width at half maximum of a peak:

$$d = \frac{K\lambda}{\beta \cos\theta} \tag{7}$$

where d is the mean crystallite size in nm, K is a dimensionless shape factor (0.94), λ is the diffraction wavelength in nm, β is the full width at half maximum in radians and θ is the Bragg angle in radians. Assuming Gaussian peak profiles and spherical crystals with cubic symmetry, the mean crystallite sizes were calculated to be 35.28, 36.90, 37.10 and 38.61 nm for the peaks of 36.29°, 38.93°, 43.16° and 54.28°, respectively.

Discharge profiles as a function of rate of prepared zinc foam on platinum at − 2.0 V and at ambient temperature with charge passed of 3000 C is seen in Figure 7. Flat discharge-profile plateaus at − 1.375 to − 1.1 V and specific capacities of $719.2 \pm 12.1\ mAh\ g^{-1}$ corresponding to a consistent coulombic efficiency of $87.7 \pm 1.5\%$ at discharge rates from 2C to C/10 were measured. The discharge profiles of zinc foam showed no significant decrease in discharge capacity at 100% depth-

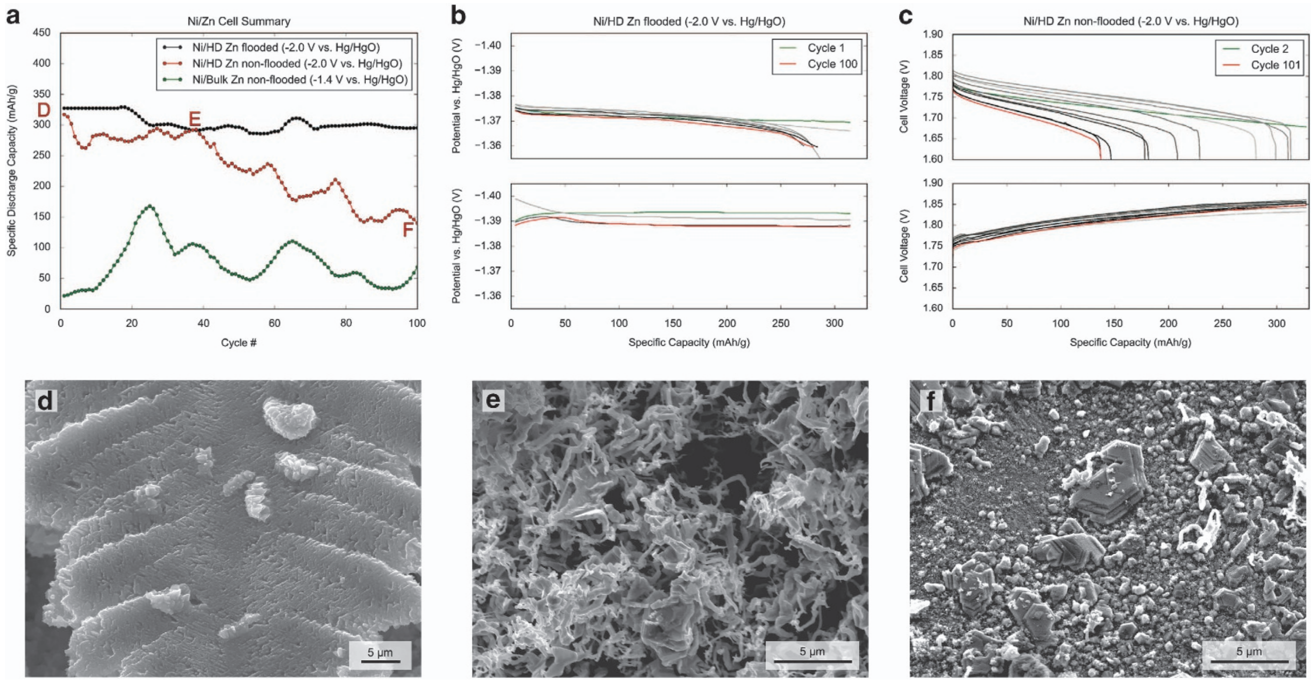

Figure 8 (**a**) Cell summary of flooded and non-flooded zinc electrodes cycled against conventional nickel electrodes over 100 cycles. (**b**) Galvanostatic charge–discharge cycling profiles of hyper-dendritic nanoporous zinc foam in a flooded cell at a rate of C/5 to a capacity limit of 40% DOD. (**c**) Galvanostatic charge–discharge cycling profiles of hyper-dendritic nanoporous zinc foam in a non-flooded cell at a rate of C/5 to a capacity limit of 40% DOD. SEM images taken from the non-flooded zinc cell at 0 (**d**), 40 (**e**) and 100 cycles (**f**).

of-discharge (DOD) and at high rates. The decrease in the voltage plateau at high discharge rates was directly correlated to higher ohmic resistance. The high utilization of the hyper-dendritic nanoporous zinc foam showed great rate capability and was comparable to results of conventional zinc anodes in a sponge form-factor.[13,33]

Conventional zinc anodes usually consist of active material, additives to suppress hydrogen and control the morphological uniformity of zinc deposition, and polymeric binders to keep zinc particles intact.[1,23,27,34] In this work, the zinc foam was prepared, *in situ*, by reducing zincate ions on a current collector with no other necessary compounds. The structural foam provided mechanical strength with an interconnected zinc current pathway throughout the core when cycled. For proof-of-concept of the hyper-dendritic zinc foam reversibility in both flooded and non-flooded systems, the zinc foam was charge–discharge cycled against a conventional nickel electrode in a full cell. At the working electrode, the reversible reaction seen in (1) took place upon charging and discharging. The active material was initially prepared by electrodeposition of zinc on nickel mesh at -2.0 V for the zinc foam and -1.4 V for the bulk or 'equilibrium' zinc, both with a charge passed of 3000 C controlled through chronocoulometry. The three-dimensional dendritic structure of nanoporous zinc on nickel mesh was confirmed under a SEM, seen in Figure 8d, and Wang *et al.*[16] results support that zinc deposits on face-centered cubic nickel substrates with no structural misfits. The capacity of the nickel counter electrode was roughly five times higher than the working electrode to ensure no capacity limitations. The prototype cells were cycled at rate of C/5 corresponding to a current of 166.67 mA, and to 40% DOD which is equivalent to a theoretical specific capacity of 328 mAh/g, to ensure that the core dendritic structure was intact. A 15-min rest between each charge and discharge step and a voltage cutoff during discharge at -1.35 V vs Hg/HgO or 1.6 V vs $Ni(OH)_2$/NiOOH was used. Figure 8a shows the summarized cycling data of the specified electrodeposited zinc up to 100 cycles, and Figures 8b and c present the charge-discharging curves for the flooded and non-flooded hyper-dendritic zinc cells. The flooded cell was less constrained than the non-flooded cells, therefore the solubility of zincate never reached a saturation point. *Ex-situ* SEM images taken at the cycle number points of 0, 40 and 100 from the non-flooded cell are seen in Figures 8d–f, respectively. The dendritic zinc foam was cycling toward equilibrium and the electrodes after 40 cycles exhibited no dendrites at macroscale. Instead, a more densified texture was evident where primary or secondary dendrites were no longer evident but rather the well-reported 'ramified' morphology. Additionally, upon cycling no precipitation of visible ZnO was formed. The hypothesis of a more dense structure over cycles of the hyper-dendritic foam was supported both by the microscopic evidence of morphology change presented, and by the shift in the open circuit potential measured at the start of the charging. Similar to the trend in Figure 4, the open circuit potential was lower for the foam architecture, thus the charge–discharge trend over cycles indicated a densification of the foam to bulk structures. This indicates that if a cell starts with metallic zinc that was formed *further* from equilibrium than the average cycling protocol demands, the zinc will restructure to form a more dense morphology, filling 'inwards', before creating ramified structures, typically misstated as dendrites. The discharge voltage profile for the flooded cell showed promising stability with less than ~1% potential fade per cycle, a specific discharge capacity of $303.1 \pm 24.9\ \mathrm{mAh\ g^{-1}}$, and low resistive losses across the cell over time (0.4–0.8 Ω). At the 100th cycle, a specific discharge capacity of $282.3\ \mathrm{mAh\ g^{-1}}$ was achieved corresponding to 86.1% of the initial capacity. For the non-flooded cells, the hyper-dendritic zinc was compared with equilibrium processed zinc (-1.4 V vs Hg/HgO) (Supplementary Figure S2), and presented superior capacity retention over 100 cycles.

CONCLUSION

We have introduced a method of synthesizing inexpensive three-dimensional zinc anodes in the form-factor of hyper-dendritic nanoporous foam, *in situ*. The zinc foam exhibits stable primary anode performance at high coulombic efficiency (87.7 ± 1.5%) and secondary anode performance beyond 100 cycles at 40% DOD. The superior performance is attributed to the three-dimensional dendritic matrix at nanoscale formed by branch growth on secondary dendrites. The branch formation resulted in zinc nanoparticles with a size distribution of 54.1–96.0 nm. The achieved nanoparticles contributed to: more rapid kinetics in comparison with conventional bulk zinc of the redox chemistry, 10–25 times larger specific surface area than bulk zinc, a 2.8 °C decrease in melting point in comparison with bulk zinc and highly oriented zinc deposition. Most interesting is that operating mesoscale isotropic three-dimensional network of dendrites far from equilibrium seems to densify the structure at standard battery operating conditions, as evidenced by the morphological change, and the shift in open circuit potential from hyper-dendritic zinc foam as a function of cycle number. This is in contrast to most literature work with zinc which starts flat or packed and seeks to emulate the 'equilibrium condition'. If hyper-dendritic structures can be recreated locally *in operando*, then a battery with a zinc anode capable of indefinite cycle life may be possible. Perhaps, if dendritic behavior can be maximized and controlled *locally*, then it may deter system limiting short circuits *globally*, as the system will move toward more dense structures as opposed to more branched structures.

CONFLICT OF INTEREST

The authors declare no conflict of interest.

ACKNOWLEDGEMENTS

This work was partially supported in part by the National Science Foundation No. 1402872 and the Department of Energy Advanced Research Projects Agency for Energy Award DE-AR0000400. C Erdonmez and M Chamoun were partially supported by Laboratory Directed Research and Development Program of Brookhaven National Laboratory (LDRD-BNL) Under Contract No. DE-AC02-98CH 10866 with the US Department of Energy. We would like to thank Dr Josh Gallaway for stimulating discussion on the nature of the diffusion layer at the limiting current, as well as Ms. Alla Zamarayeva for encouragement to studying the electrochemical properties of this curious morphology.

---

1 McBreen, J. Zinc electrode shape change in secondary cells. *J. Electrochem. Soc.* **119**, 1620–1628 (1972).

2 Falk, S. U. & Salkind, A. J. *Alkaline Storage Batteries* (John Wiley, New York, NY, USA, 1969).

3 Tomazic, G. Zinc-bromine battery with circulating electrolytes. *J. Power Sources* **70**, 168 (1998).

4 Singh, P. & Jonshagen, B. Zinc-bromine battery for energy storage. *J. Power Sources* **35**, 405–410 (1991).

5 Smedley, S. I. & Zhang, X. G. A regenerative zinc–air fuel cell. *J. Power Sources* **165**, 897–904 (2007).

6 Steingart, D. A. & Evans, J. W. Measurements of granular flows in two-dimensional hoppers by particle image velocimetry. Part I: experimental method and results. *Chem. Eng. Sci.* **60**, 1043–1051 (2005).

7 Ito, Y., Nyce, M., Plivelich, R., Klein, M. & Steingart, D. Zinc morphology in zinc–nickel flow assisted batteries and impact on performance. *J. Power Sources* **196**, 2340–2345 (2011).

8 Cachet, C., Saidani, B. & Wiart, R. The behavior of zinc electrode in alkaline electrolytes: II. A kinetic analysis of anodic dissolution. *J. Electrochem. Soc.* **139**, 644–654 (1992).

9 Arouete, S., Blurton, K. F. & Oswin, H. G. Controlled current deposition of zinc from alkaline solution. *J. Electrochem. Soc.* **116**, 166–169 (1969).

10 Shen, Y. & Kordesch, K. The mechanism of capacity fade of rechargeable alkaline manganese dioxide zinc cells. *J. Power Sources* **87**, 162–166 (2000).

11 Gallaway, J. W., Erdonmez, C. K., Zhong, Z., Croft, M., Sviridov, L. A., Sholklapper, T. Z., Turney, D. E., Banerjee, S., Steingart, D. A. Real-time materials evolution visualized within intact cycling alkaline batteries. *J. Mater. Chem. A Mater. Energy Sustain* **2**, 2757–2764 (2014).

12 López, C. M. & Choi, K.-S. Electrochemical synthesis of dendritic zinc films composed of systematically varying motif crystals. *Langmuir* **22**, 10625–10629 (2006).

13 Parker, J. F., Chervin, C. N., Nelson, E. S., Rolison, D. R. & Long, J. W. Wiring zinc in three dimensions re-writes battery performance—dendrite-free cycling. *Energy Environ. Sci.* **7**, 1117–1124 (2014).

14 Linden, D. & Reddy, T. B. *Handbook of Batteries* (McGraw-Hill, New York, NY, USA, 2002).

15 Cho, Y.-D. & Fey, G. T.-K. Surface treatment of zinc anodes to improve discharge capacity and suppress hydrogen gas evolution. *J. Power Sources* **184**, 610–616 (2008).

16 Wang, R. Y., Kirk, D. W. & Zhang, G. X. Effects of deposition conditions on the morphology of zinc deposits from alkaline zincate solutions. *J. Electrochem. Soc.* **153**, C357–C364 (2006).

17 Naybour, R. D. Morphologies of zinc electrodeposited from zinc-saturated aqueous alkaline solution. *Electrochim. Acta* **13**, 763–769 (1968).

18 McLarnon, F. R. & Cairns, E. J. The secondary alkaline zinc electrode. *J. Electrochem. Soc.* **138**, 645–656 (1991).

19 Witten, T. A. & Sander, L. M. Diffusion-limited aggregation, a kinetic critical phenomenon. *Phys. Rev. Lett.* **47**, 1400–1403 (1981).

20 Matsushita, M., Sano, M., Hayakawa, Y., Honjo, H. & Sawada, Y. Fractal structures of zinc metal leaves grown by electrodeposition. *Phys. Rev. Lett.* **53**, 286–289 (1984).

21 Grier, D., Ben-Jacob, E., Clarke, R. & Sander, L. M. Morphology and microstructure in electrochemical deposition of zinc. *Phys. Rev. Lett.* **56**, 1264–1267 (1986).

22 Cachet, C., Saïdani, B. & Wiart, R. The behavior of zinc electrode in alkaline electrolytes: I. A kinetic analysis of cathodic deposition. *J. Electrochem. Soc.* **138**, 678–687 (1991).

23 McBreen, J., Gannon, E., Chin, D. T. & Sethi, R. Zinc electrode morphology in alkaline solutions: II. Study of alternating charging current modulation on pasted zinc battery electrodes. *J. Electrochem. Soc.* **130**, 1641–1645 (1983).

24 Dirkse, T. P. & Hampson, N. A. The anodic behaviour of zinc in aqueous KOH solution—II. Passivation experiments using linear sweep voltammetry. *Electrochim. Acta* **17**, 387–394 (1972).

25 Dirkse, T. P. The behavior of the zinc electrode in alkaline solutions. II. Reaction orders at the equilibrium potential. *J. Electrochem. Soc.* **126**, 541–543 (1979).

26 Rogers, G. T. & Taylor, K. J. A rotating disc electrode study of the electrodeposition of zinc from alkaline zincate solutions. *J. Electroanal. Chem. Interfacial Electrochem.* **167**, 251–264 (1984).

27 Karpinski, A. P., Makovetski, B., Russell, S. J., Serenyi, J. R. & Williams, D. C. Silver–zinc: status of technology and applications. *J. Power Sources* **80**, 53–60 (1999).

28 Moshtev, R. V. & Zlatilova, P. Kinetics of growth of zinc dendrite precursors in zincate solutions. *J. Appl. Electrochem.* **8**, 213–222 (1978).

29 Despic, A. R., Diggle, J. & Bockris, J. O. Mechanism of the formation of zinc dendrites. *J. Electrochem. Soc.* **115**, 507–508 (1968).

30 Osório, W. R., Spinelli, J. E., Cheung, N. & Garcia, A. Secondary dendrite arm spacing and solute redistribution effects on the corrosion resistance of Al–10 wt% Sn and Al–20 wt% Zn alloys. *Mater Sci Eng A* **420**, 179–186 (2006).

31 Jiang, Q. & Lu, H. M. Size dependent interface energy and its applications. *Surf. Sci. Rep.* **63**, 427–464 (2008).

32 Roeber, E. F. & Parmelee, H. C. *Electrochemical and Metallurgical Industry* (Electrochemical Publishing Company, 1907).

33 Zhang, X. G. Fibrous zinc anodes for high power batteries. *J. Power Sources* **163**, 591–597 (2006).

34 Salkind, A. J., Karpinski, A. P. & Serenyi, J. R. in *Encyclopedia of Electrochemical Power Sources*, 513–523 (Elsevier, 2009).

Supplementary Information accompanies the paper on the NPG Asia Materials website (http://www.nature.com/am)